Water Research X 16 (2022) 100153

Contents lists available at ScienceDirect

Water Research X

journal homepage: www.sciencedirect.com/journal/water-research-x

Removal of soluble divalent manganese by superfine powdered activated carbon and free chlorine: Development and application of a simple kinetic model of mass transfer–catalytic surface oxidation

Shun Saito [a,b], Yoshihiko Matsui [c,*], Nobutaka Shirasaki [c], Taku Matsushita [c]

[a] Graduate School of Engineering, Hokkaido University, N13W8, Sapporo 060-8628, Japan
[b] Metawater Co., Ltd., Kandasuda-cho 1-25, Chiyoda-ku, Tokyo 101-8554, Japan
[c] Faculty of Engineering, Hokkaido University, N13W8, Sapporo 060-8628, Japan

ARTICLE INFO

Keywords:
Activated carbon
Oxidation
Adsorption
Film mass transfer
Eley-Rideal

ABSTRACT

Catalytic oxidative removal of Mn^{2+} on activated-carbon surfaces by free chlorine was recently discovered and found to be potentially practicable for water treatment when using micrometer-sized activated carbon. Herein, we newly derived a kinetic model for trace-substance removal by catalytic reaction and applied it to the Mn^{2+} removal. External-film mass transfer, adsorption, and oxidation/desorption contributed similarly to the Mn^{2+} removal rate under actual practical conditions. The low removal rate in natural water was attributed to decreases in available adsorption sites: e.g., a 50% decrease in available sites in water with 0.26 mmol-Ca^{2+}/L caused a 15% reduction in removal rate. Low temperature greatly reduced the removal rate by both enhancing the decrease in available sites and hindering mass transfer through increased viscosity. While adsorption sites differed 8-fold between different carbon particles, causing a 2.2-fold difference in removal rates, carbon particle size was more influential, with a >10-fold difference between 2- and 30-μm sizes.

1. Introduction

In municipal water supplies, the divalent manganese ion (Mn^{2+}), which is oxidized to black manganese oxides (MnO_X) in distribution systems, is a main cause of esthetic problems in drinking water (Civardi and Tompeck, 2015; Gerke et al., 2016; Li et al., 2019b; Riddick et al., 1958; Sly et al., 1990; Tobiason et al., 2016). In a conventional treatment system including rapid sand filtration, Mn^{2+} is removed in a process in which a coating of MnO_X on the surface of filter sand acts as a catalyst, and Mn^{2+} is oxidized and precipitated on the MnO_X in the presence of free chlorine (Hu et al., 2004; Jones et al., 2018; Knocke et al., 1991; Singer and Reckhow, 2011; Tobiason et al., 2008). In other treatment systems such as membrane filtration, however, this approach does not work because there is no medium like sand that can be coated with MnO_X.

In such a situation, in a membrane filtration pilot experiment, we discovered that Mn^{2+} was removed to below the quantification limit by superfine powdered activated carbon (SPAC; particle size of less than a few micrometers) in the presence of free chlorine (Saito et al., 2020). A little earlier, Li et al. (2019a) also reported the catalytic effect of powdered activated carbon (PAC; particle size of tens of micrometers) on Mn^{2+} oxidation by free chlorine. Although activated carbon has been known as a catalyst for oxidation (Ahumada et al., 2002; Faria et al., 2009; Gomes et al., 2010; Moreno-Castilla et al., 2000), we believe that its catalytic effect on Mn^{2+} oxidation had probably not yet been found because of its limited catalytic activity. Moreover, traditional drinking-water treatment approaches would avoid any direct interaction between activated carbon and free chlorine because of the reductive tendencies of the carbon to the free chlorine. However, the use of small particles (SPAC) would compensate for the weak catalytic activity and provide sufficient Mn^{2+} removal performance even with a short reaction time, and this approach has been demonstrated to be practicable as a drinking-water treatment method (Saito et al., 2020).

The removal of Mn^{2+} by activated carbon and free chlorine follows first-order reaction kinetics (Eq. (1)) (Li et al., 2019a; Saito et al., 2020). However, the theoretical basis for this apparent kinetics remains uncertain, and to date there is no analysis of the removal kinetics or mechanism.

$$\ln\left(C_M / C_{0,M}\right) = -k\,t \quad (1)$$

In contrast to activated carbon, there are kinetic studies of catalytic

* Corresponding author.
E-mail address: matsui@eng.hokudai.ac.jp (Y. Matsui).

https://doi.org/10.1016/j.wroa.2022.100153
Received 8 May 2022; Received in revised form 1 August 2022; Accepted 4 August 2022
Available online 5 August 2022

Nomenclature

A	external-film area of a catalyst per volume of water (m^2/m^3)
$C_{E,M}$	concentration of an oxidation target just above the surface of a catalyst (mol/m^3)
$C_{E,Oxid}$	oxidant concentration just above the surface of a catalyst (mol/m^3)
C_M	bulk-phase concentration of an oxidation target (mol/m^3)
C_{Oxid}	bulk-phase oxidant concentration (mol/m^3)
C_S	dosage of a catalyst (g/m^3)
C_{Site}	reactive-site concentration on a catalyst (mol/m^2)
$C_{0,M}$	initial concentration of bulk-phase oxidation target (mol/m^3)
d_L	diameter of a particle as determined by a laser-light diffraction method (m)
d_V	equivalent volume diameter of a particle (m)
$D_{L3,2}$	Sauter mean particle diameter determined by a laser-light diffraction method (m)
D_S	volume-surface mean diameter (m)
D_W	diffusion coefficient of an oxidation target in water (m^2/s)
$fun(q_M)$	function of adsorbed-phase concentration of an oxidation target as an isotherm equation (mol/m^3)
G	mixing intensity defined as the square root of the value; energy dissipation divided by fluid viscosity (s^{-1})
k	removal-rate coefficient of the pseudo-first-order reaction (s^{-1})
k_A	adsorption rate coefficient [$m^3/(mol\ s)$]
k_D	desorption rate coefficient (s^{-1})
k_F	rate coefficient of external-film mass transfer (m/s)
k_{Oxid}	oxidation reaction rate coefficient [$m^3/(mol\ s)$]
K_R	overall reaction rate coefficient (m/s)
q_{Max}	maximum mass of adsorbed-phase oxidation target per unit of media surface (mol/m^2)
q_M	mass of adsorbed-phase oxidation target per unit of media surface (mol/m^2)
R_A	rate of adsorption [$mol/(m^2\ s)$]
R_D	rate of desorption [$mol/(m^2\ s)$]
R_F	rate of external-film mass transfer [$mol/(m^2\ s)$]
R_{Oxid}	rate of oxidation reaction [$mol/(m^2\ s)$]
R_R	rate of removal [$mol/(m^3\ s)$]
s_P	external surface area of a particle (m^2)
Sh	Sherwood number (dimensionless)
t	time of reaction (s)
v_P	volume of a particle (m^3)
ε	power dissipated per unit mass of water (m^2/s^3)
θ_C	site coverage by co-existing substances other than an oxidation target (dimensionless)
θ_M	site coverage by an oxidation target (dimensionless)
ρ	density of a catalyst particle (g/m^3)
σ	kinematic viscosity of water (m^2/s)
φ	Wadell's sphericity (dimensionless)
$\varnothing$	ratio of d_L to d_V (dimensionless)

Mn^{2+} oxidation on MnO_X surfaces by free chlorine, the earliest in 1967 (Nakanishi, 1967). Nakanishi proposed the model that Mn^{2+} is initially adsorbed on the MnO_X surface, and then the adsorbed Mn^{2+} is catalytically oxidized by free chlorine. The rate of Mn^{2+} removal and the mass balance for the adsorbed-phase Mn^{2+} on the MnO_X surface in the Nakanishi model are as follows:

$$R_R = k_A C_M (q_{Max} - q_M) - k_D q_M \tag{2}$$

$$\frac{dq_M}{dt} = k_A C_M (q_{Max} - q_M) - k_D q_M - k_{Oxid} q_M C_{Oxid} \tag{3}$$

After referencing the Nakanishi model, Merkle et al. (1997) proposed a dynamic model that considered the external-film mass transfer of Mn^{2+} to the MnO_X surface (Eq. (4)). They assumed the local equilibrium of the Freundlich adsorption isotherm in the Mn^{2+} adsorption process. The basics of the Merkle model have been followed in later studies (Bierlein et al., 2015; Kenari et al., 2019).

$$R_R = -k_F (C_M - C_{E,M}) \tag{4}$$

The local equilibrium of Mn^{2+} adsorption on the MnO_X surface was expressed as

$$C_{E,M} = fun(q_M) \tag{5}$$

The mass balance equation for the adsorbed-phase Mn^{2+} on the MnO_X surface is as follows:

$$\frac{dq_M}{dt} = k_F (C_M - C_{E,M}) - k_{Oxid}\ q_M C_{Oxid} \tag{6}$$

The Markle model is superior to the Nakanishi model in that it is capable of describing the change in the Mn^{2+} removal rate with fluid conditions. In this model, it is necessary to assume that either the mass transfer or the oxidation reaction is the rate-limiting step to derive the pseudo-first-order reaction rate characteristics that are observed with activated carbon as a catalyst (Li et al., 2019a; Saito et al., 2020). On the other hand, the rate coefficient of Mn^{2+} removal by activated carbon is little affected by differences in free chlorine concentration, especially in the high concentration range (Saito et al., 2020), but it is affected by the presence of co-existing substances (explained in Section 4.1) and the mixing intensity of the reactor (explained in Section 4.2). These dependencies of the removal rate cannot be explained by the Merkle model with the rate-limiting-step assumption. Therefore, these models are not applicable to Mn^{2+} removal by activated carbon and free chlorine.

In researching heterogeneous catalysis on solid catalyst surfaces, the Langmuir adsorption isotherm is generally used for the kinetic analysis (Baxter and Hu, 2002; Boudart and Djega-Mariadassou, 2014; Chorkendorff and Niemantsverdriet, 2007). In reactions involving two molecules, the case where both molecules adsorb to an adsorption site for the subsequent reaction is called the Langmuir-Hinshelwood mechanism, whereas the case where one molecule adsorbs to an adsorption site, and then reacts directly with another molecule in the gas or liquid phase, is called the Eley-Rideal (ER) mechanism (Misono, 2013; Prins et al., 2016; Ross, 2012a). These two mechanisms have been used in many studies of catalytic reaction kinetics. Although the rate of mass transfer may also affect the overall reaction rate, most research dealing with gas–solid catalytic reactions have focused on the chemical reactions on the catalyst surface because the rate of mass transfer is much faster than the chemical reaction (Gómez-Marín and Hernández-Ortiz, 2014; Ross, 2012b).

On the other hand, the oxidative Mn^{2+} removal targeted in this study is a liquid–solid reaction, where the mass transfer through an external film by diffusion is much slower than in a gas–solid reaction because of much higher fluid viscosity. It is therefore appropriate to analyze the reaction rate taking into account the effects of mass transfer. In some studies of liquid–solid reactions, however, the focus has been on the chemical reaction, concluding through qualitative discussion that the external-film mass-transfer rate is negligible (Al-Sakkari et al., 2017; Chantrasa et al., 2011; Dhawane et al., 2021). There have been studies that considered the contribution of the external-film mass transfer in catalytic reactions (Ercan et al., 1998; Hatziantoniou et al., 1986; Satterfield, 1969), but the overall reaction rate in first-order-reaction form

has not been derived.

Thus, we could not find any kinetic study that fit the catalytic oxidation of Mn^{2+} by activated carbon and free chlorine that also follows the first-order reaction-rate law. In the present study, we developed an overall kinetic model in the form of a first-order reaction for the catalytic oxidation of trace substances, such as the oxidation of Mn^{2+} in water by activated carbon in the presence of free chlorine, considering external-film mass transfer and the ER mechanism. In addition, we used the developed model to quantitatively analyze the kinetics of Mn^{2+} removal by SPAC and free chlorine.

2. Theorical development

2.1. Overall rate of trace-substance surface oxidation

The rate of mass transfer of an oxidation target (Mn^{2+} in this study) across an external film by molecular diffusion is

$$R_F = k_F\left(C_M - C_{E,M}\right) \tag{7}$$

We applied the ER mechanism to describe the kinetics of catalytic processes of the oxidation target on the catalyst surface (Ross, 2012a).

Adsorption rate:

$$R_A = k_A C_{E,M} C_{Site}(1 - \theta_M - \theta_C) \tag{8}$$

Desorption rate:

$$R_D = k_D C_{Site}\theta_M \tag{9}$$

Oxidation rate:

$$R_{Oxid} = k_{Oxid} C_{E,Oxid} C_{Site}\theta_M \tag{10}$$

The quasi-steady-state approximation for the adsorption, desorption, and oxidation is applied by assuming that the net adsorption–desorption rate ($R_A - R_D$) is equal to the oxidation rate (R_{Oxid}). This assumption is valid when the amount of reaction intermediate (adsorbed target substance, $C_{Site}\theta_M$) changes instantaneously depending on $C_{E,M}$ because the adsorption-site concentration on a catalyst surface (C_{Site}) is low.

$$k_A C_{E,M} C_{Site}(1 - \theta_M - \theta_C) - k_D C_{Site}\theta_M = k_{Oxid} C_{E,Oxid} C_{Site}\theta_M \tag{11}$$

Adsorptive Mn^{2+} removal by SPAC alone is not significant (Saito et al., 2020). Even after SPAC was pre-oxidized by free chlorine, Mn^{2+} removal was not evident when free chlorine was absent at the time of the reaction (Fig. S1). These results confirm the very low adsorption capacity (C_{Site}) of activated carbon (catalyst) for Mn^{2+} (oxidation target), supporting the quasi-steady-state approximation.

Because the catalytic oxidation of Mn^{2+} proceeds on the outer (external) surface of activated carbon (Saito et al., 2020), internal diffusion of Mn^{2+} in an activated-carbon particle is not considered. We also applied the quasi-steady-state approximation for the mass transfer and the net adsorption–desorption rate ($R_F = R_A - R_D$).

$$k_F\left(C_M - C_{E,M}\right) = k_A C_{E,M} C_{Site}(1 - \theta_M - \theta_C) - k_D C_{Site}\theta_M \tag{12}$$

From Eqs. (10) and (11), the overall reaction rate ($R_R \equiv R_F = R_A - R_D = R_{Oxid}$) is given by

$$R_R = \frac{k_A k_{Oxid}\ C_{E,Oxid} C_{E,M} C_{Site}(1 - \theta_C)}{k_A C_{E,M} + k_{Oxid} C_{E,Oxid} + k_D} \tag{13}$$

The condition of $k_A C_{E,M} << k_{Oxid} C_{E,Oxid} + k_D$ can be assumed when the concentration of an oxidation target (Mn^{2+}, $C_{E,M}$) is low compared with the oxidant concentration (free chlorine, $C_{E,Oxid}$). In that case,

$$R_R = \frac{k_A k_{Oxid}\ C_{E,Oxid} C_{E,M} C_{Site}(1 - \theta_C)}{k_{Oxid} C_{E,Oxid} + k_D} \tag{14}$$

Combining Eqs. (12) and (14) and rearranging, the resultant equation is

$$C_{E,M} = C_M \frac{1}{1 + \frac{k_A k_{Oxid}\ C_{E,Oxid} C_{Site}(1-\theta_C)}{k_F\left(k_{Oxid} C_{E,Oxid} + k_D\right)}} \tag{15}$$

Substituting Eq. (15) into Eq. (7), the overall removal reaction rate (R_R) becomes

$$R_R = K_R\ C_M \tag{16}$$

Here, K_R is the overall reaction rate coefficient defined as follows:

$$\frac{1}{K_R} \equiv \frac{1}{k_F} + \frac{1}{k_A C_{Site}(1 - \theta_C)} + \frac{k_D}{k_A k_{Oxid} C_{Site}(1 - \theta_C)} \frac{1}{C_{E,Oxid}} \tag{17}$$

Under conditions where $C_M \ll C_{Oxid}$, the decrease in C_{Oxid} is minimal because oxidant (free chlorine) consumption by the target substance (Mn^{2+}) oxidation reaction is very small. In addition, the external-film mass-transfer rate of the oxidant is greater than that of the oxidation target because of its higher concentration than the oxidation target. Therefore, the mass-transfer rate of the oxidant should not be a rate-limiting step for influencing the overall reaction rate. Thus, $C_{E,Oxid} \cong C_{Oxid}$, and

$$\frac{1}{K_R} \equiv \frac{1}{k_F} + \frac{1}{k_A C_{Site}(1 - \theta_C)} + \frac{k_D}{k_A k_{Oxid} C_{Site}(1 - \theta_C)} \frac{1}{C_{Oxid}} \tag{18}$$

Consequently, the overall kinetic model for removal expressed with a first-order reaction rate, which was observed experimentally, is derived theoretically, and the overall reaction rate coefficient can be represented by a linear combination of the three rate resistances, i.e., those due to external-film mass transfer, adsorption, and oxidation/desorption.

2.2. Batch reaction

The mass balance of Mn^{2+} in a reactor is

$$\frac{dC_M}{dt} = -AR_F = -AK_R\ C_M \tag{19}$$

Here, A is the external-film area of activated carbon per volume of water, which is defined as

$$A \equiv \frac{C_S}{\rho}\frac{6}{D_S} \tag{20}$$

D_S is the volume-surface mean diameter of an activated-carbon particle, obtained by the equivalent volume diameter of a particle (d_V) and the Wadell's sphericity (φ) as follows:

$$D_S = \frac{6\sum v_P}{\sum s_P} = \frac{\sum {d_V}^3}{\sum {d_V}^2/\varphi} \tag{21}$$

We used a laser-light diffraction (LD) method to determine activated-carbon particle size (explained in Section 3.1). We introduce the ratio $\varnothing$ to consider the difference between the LD diameter (d_L) and d_V (Eshel et al., 2004):

$$\varnothing = d_V/d_L \tag{22}$$

Substituting Eq. (22) in Eq. (21) yields

$$D_S = \varphi\varnothing D_{L3,2} \tag{23}$$

$D_{L3,2}$ can be calculated from the output result of the LD measurement:

$$D_{L3,2} \equiv \frac{\sum {d_L}^3}{\sum {d_L}^2} \tag{24}$$

Integrating Eq. (19) and substituting the boundary conditions for the batch reaction of $t = 0$ and $C_M = C_{0,\,M}$, the change of Mn^{2+} concentration in the batch reactor is expressed as follows:

$$\ln\left(C_M / C_{0,M}\right) = -AK_R\ t \tag{25}$$

Table 1
Carbons used in the present study.

Designation	$D_{L3,2}$ in stock bottle (μm)	$D_{L3,2}$ in dispersed state (μm)	Raw material	Product name	Related experimental runs
SPAC-A1	2.21	1.07	Wood	Taiko W [1]	Runs 1–7, 9, 10
SPAC-A2	3.15	3.01	Wood	Taiko W	Run 8
PAC-B	30.1	21.8	Wood	Taiko W	Runs 11, 12
SPAC-B1	8.79	8.77	Wood	Taiko W	Runs 11, 12
SPAC-B2	4.51	4.45	Wood	Taiko W	Runs 11, 12
SPAC-B3	3.10	2.14	Wood	Taiko W	Runs 11, 12
SPAC-B4	3.14	1.14	Wood	Taiko W	Runs 11, 12
SPAC-B5	2.75	0.71	Wood	Taiko W	Runs 11, 12
SSPAC-B1	2.87	0.39	Wood	Taiko W	Run 12
SSPAC-B2	3.41	0.16	Wood	Taiko W	Run 12
SSPAC-B3	3.04	0.16	Wood	Taiko W	Run 12
SPAC-C	1.27	0.74	Wood	Taiko W	Run 13
SPAC-D	2.13	0.95	Wood	Shirasagi C-1 [2]	Run 13
SPAC-E	1.82	1.00	Wood	LP-WPS [3]	Run 13
SPAC-F	1.65	1.36	Coal	6D [4]	Run 13
SPAC-G	2.97	0.95	Coal	Diahope XPS [4]	Run 13
SPAC-H	2.12	0.92	Coconut	Taiko HW [1]	Run 13
Charcoal	2.01	0.82	Oak	No brand	Run 13

[1] Futamura Chemical Co., Ltd.
[2] Osaka Gas Chemicals Co., Ltd.
[3] Dainen Co., Ltd.
[4] Calgon Carbon Corporation (via Kuraray Co., Ltd.).

3. Materials and methods

3.1. Carbons

We collected five wood-based, two coal-based, and one coconut-based commercial PAC as well as one charcoal. SPAC and submicron-SPAC (SSPAC) were produced by micro-milling each original PAC or charcoal. Details of the micro-milling procedure are described in Text S1 (Saito et al., 2020; Takaesu et al., 2019; Zhao et al., 2020). Table 1 summarizes the carbons used. The particle sizes of the carbons were determined by means of an LD method (Microtrac MT3300EXII; MicrotracBEL Corp., Osaka, Japan). To determine the particle sizes in their state in a stock suspension, each carbon suspension (2 g/L) was directly introduced from the stock bottle to the circulation system (Mictrotrac Sample Delivery Controller; MicrotracBEL Corp.) attached to the measurement equipment (the mass of carbons introduced to the circulation system were 2–10 mg). We also determined the dispersed-state particle sizes by adding a dispersant (Triton X-100; Kanto Chemical Co., Tokyo, Japan; final concentration, 0.08% w/v) with subsequent ultrasonication (150 W, 19.5 kHz) for 1 min (US-300E; Nihonseiki Kaisha Ltd., Tokyo, Japan) prior to introducing the suspension to the circulation system. Representative particle-size distributions are shown in Fig. S2.

3.2. Water samples

The characteristics of the waters used in the experiments are summarized in Table 2. Waters 1 and 2 were natural waters that were collected at the Moiwa Water Purification Plant (Sapporo Waterworks Bureau, Japan) that receives Toyohira River water (Sapporo City, Hokkaido, Japan). The remaining waters included additions of one or more stock solutions. A Mn^{2+} stock solution was prepared by dissolving $MnCl_2{\cdot}4H_2O$ (Guaranteed Reagent, Fujifilm Wako Pure Chemical Corporation, Osaka, Japan) in a 0.1 mEq/L solution of sulfuric acid (H_2SO_4) or hydrochloric acid (HCl) at a concentration of 100 mg-Mn/L (1.82 mol-Mn/m^3). $CaCl_2$ stock solution was prepared by dissolving $CaCl_2$ (Guaranteed Reagent, Fujifilm Wako Pure Chemical Corporation) in ultrapure water (Milli-Q Advantage A10, Merck KGaA, Darmstadt, Germany) at a concentration of 250 mol-Ca/m^3, followed by membrane filtration (0.2-μm pore size; DISMIC 25HP020AN; Toyo Roshi Kaisha, Ltd., Tokyo, Japan). Suwanee River natural organic matter (SRNOM) powder (1R101N; International Humic Substances Society, Denver, Colorado, USA) was added to ultrapure water to prepare an SRNOM stock solution with a dissolved organic carbon (DOC, an index of dissolved natural organic matter) concentration 200 mg/L.

Table 2
Characteristics of the waters used in the present study. All measurements except turbidity and alkalinity were taken after membrane filtration.

Water	Description	Turbidity NTU	UV260 AU	DOC mg/L	Mn^{2+} μg/L (mmol/m^3)	Alkalinity mol/m^3	Na^+ mol/m^3	K^+ mol/m^3	Mg^{2+} mol/m^3	Ca^{2+} mol/m^3	Cl^- mol/m^3	NO_3^- mol/m^3	SO_4^{2-} mol/m^3
1	Natural water	1.9	0.118	0.85	7.7 (0.140) [1]	0.16	0.35	0.03	0.08	0.21	0.29	0.02	0.13
2	Natural water	0.5	0.125	0.87	9.8 (0.179) [1]	0.18	0.52	0.05	0.09	0.26	0.50	0.02	0.18
3	Ionic water	NM	0.000	0.04	10 (0.182)	0.18	0.60	0.05	0.09	0.26	0.57	0.03	0.20
4	Carbonate-buffered pure water	NM	0.000	0.03	10 (0.182)	0.10	0.20	0.00	0.00	0.00	0.01	0.02	0.02
5	Carbonate-buffered pure water	NM	0.000	0.03	10 (0.182)	0.10	0.20	0.00	0.00	0.00	0.01	0.02	0.00
6	Carbonate-buffered pure water	NM	0.000	0.03	50 (0.910)	0.10	0.20	0.00	0.00	0.00	0.01	0.02	0.00
7	$CaCl_2$-spiked pure water	NM	NM	NM	10 (0.182)	0.10	0.19	0.00	0.00	0.25	0.56	0.01	0.00
8	$CaCl_2$-spiked pure water	NM	NM	NM	10 (0.182)	0.10	0.18	0.00	0.00	0.50	1.16	0.02	0.00
9	$CaCl_2$-spiked pure water	NM	NM	NM	10 (0.182)	0.10	0.19	0.00	0.00	1.01	2.47	0.02	0.00
10	SRNOM-spiked ionic water	NM	0.036	0.29	10 (0.182)	0.18	0.61	0.05	0.09	0.26	0.63	0.04	0.19
11	SRNOM-spiked ionic water	NM	0.176	0.80	10 (0.182)	0.18	0.61	0.05	0.09	0.26	0.63	0.04	0.19
12	SRNOM-spiked ionic water	NM	0.315	1.47	10 (0.182)	0.18	0.61	0.05	0.09	0.26	0.61	0.04	0.18
13	SRNOM-spiked ionic water	NM	0.460	2.22	10 (0.182)	0.18	0.61	0.05	0.09	0.25	0.63	0.04	0.19
14	SRNOM-spiked ionic water	NM	0.625	3.11	10 (0.182)	0.18	0.61	0.05	0.09	0.26	0.63	0.04	0.19

NM, not measured; UV260, ultraviolet absorbance at 260 nm over 50 mm; AU, absorbance units; DOC, dissolved organic carbon; SRNOM, Suwanee River natural organic matter.
[1] The Mn^{2+} concentrations in natural waters were obtained by subtracting the concentration of colloidal Mn, which is considered to be in an oxidized state, from the total soluble Mn concentration (Carlson et al., 1997; Saito et al., 2022).

Table 3
Experimental conditions.

Run	Water used	Volume	Water temperature	Stirring speed	G value	Carbon[1]	Free chlorine dosage	pH adjustment reagent	Related figures
		m L	°C	rpm	s^{-1}		mg-Cl_2/L (mmol/m^3)		
1	1	1000	19–20	400	509	SPAC-A1	0.00–1.48 (0.0–20.9) (6 conditions)	H_2SO_4	Figs. 1, 2A, S3, S4
2	2	1000	19–20	400	509	SPAC-A1	0.00–1.47 (0.0–20.7) (6 conditions)	H_2SO_4	Figs. 1, 2B, S3, S4
3	3	1000	19–20	400	509	SPAC-A1	0.00–4.85 (0.0–68.4) (8 conditions)	H_2SO_4	Figs. 1, 2C, S3, S4
4	4	1000	19–20	400	509	SPAC-A1	0.00–4.85 (0.0–68.4) (9 conditions)	H_2SO_4	Figs. 1, 2D, S3, S4
5	7–9 (3 waters)	1000	19–20	400	509	SPAC-A1	1.00 (14.1)	HCl	Figs. S5, S6
6	3, 10–14 (6 waters)	1000	19–20	400	509	SPAC-A1	1.00 (14.1)	H_2SO_4	Figs. S5, S6
7	3	1000	19–20	50–800 (8 conditions)	23–1440	SPAC-A1	1.00 (14.1)	H_2SO_4	Figs. 3, 4C, S7
8	3	1000	19–20	50–800 (6 conditions)	23–1440	SPAC-A2	1.00 (14.1)	H_2SO_4	Figs. S8, S9
9	3	1000	3–20 (4 conditions)	400	401–509	SPAC-A1	1.00 (14.1)	H_2SO_4	Figs. 5, 6, S10
10	4	1000	4–23 (6 conditions)	400	408–528	SPAC-A1	1.00 (14.1)	H_2SO_4	Figs. 5, 6, S10
11	5	2000	19–20	400	509	PAC-B, SPAC-B1–B5 (6 carbons)	1.00 (14.1)	HCl	Figs. 7, 8, S11
12	6	2000	19–20	400	509	PAC-B, SPAC-B1–B5, SSPAC-B1–B3 (9 carbons)	1.00 (14.1)	HCl	Figs. 7, S11
13	4	1000	19–20	400	509	SPAC-C–H, Charcoal (7 carbons)	1.00 (14.1)	H_2SO_4	Figs. 8, S12

[1] The carbon dosage for all runs was 1.0 mg/L.

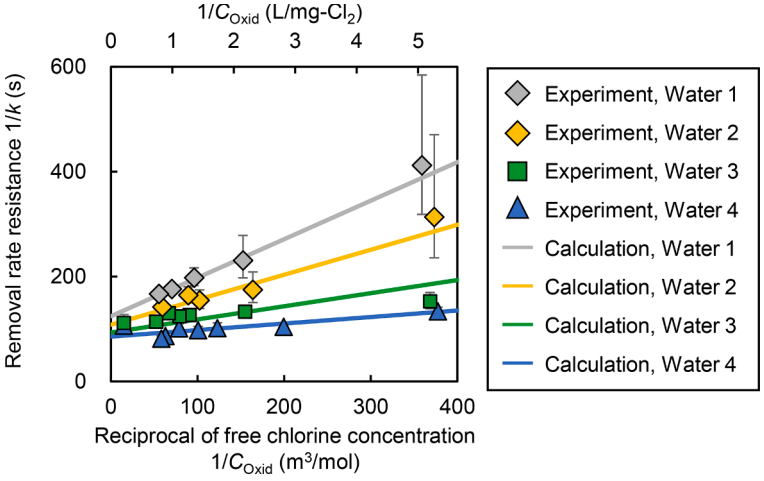

Fig. 1. Removal-rate resistance ($1/k$) as a function of free chlorine concentration, according to Eq. (1). Results from Run 1 using Water 1 (natural water); Run 2, Water 2 (natural water); Run 3, Water 3 (an ionic water with the same ion concentrations as Water 2); and Run 4, Water 4 (a carbonate-buffered pure water). SPAC-A1 was used as the carbon. Initial Mn^{2+} concentration, 7.7–10 μg/L (0.140–0.182 mmol/m^3); carbon dosage, 1.0 mg/L (1.0 g/m^3); water temperature, 19–20 °C; G, 509 s^{-1}. C_{Oxid} values are the time-averaged free chlorine concentrations during the reaction. The experimental data for k and C_{Oxid} value determinations are shown in Fig. S3. Error bars indicate 95% confidence intervals. Calculation was performed using Eq. (26) substituting the values from Table 4 for $1/Ak_F$, $1/Ak_AC_{Site}$, θ_C, and k_D/k_{Oxid}.

Table 4
Parameter values determined by fitting the model.

$\frac{1}{Ak_F}$ (s)	$\frac{1}{Ak_AC_{Site}}$ (s)	$\frac{k_D}{k_{Oxid}}$ (mol/m^3)	θ_C (dimensionless)			
			Water 1	Water 2	Water 3	Water 4
77.7	7.85	0.0158	0.831	0.740	0.503	0.000*

* a priori assumption.

Water 3 was an ion-adjusted water that was prepared by adding the Mn^{2+} stock solution, carbonate buffer ($NaHCO_3$), $CaCl_2$, $MgCl_2$, NaCl, KCl, Na_2SO_4, and HNO_3 (Guaranteed Reagents, Fujifilm Wako Pure Chemical Corporation) to ultrapure water. Waters 4–6 were carbonate-buffered pure waters that were prepared by adding the Mn^{2+} stock solution and carbonate buffer ($NaHCO_3$) to ultrapure water. Waters 7–9 were $CaCl_2$-spiked pure waters that were prepared by adding the $CaCl_2$ stock solution to Water 4 (carbonate-buffered pure water). Waters 10–14 were SRNOM-spiked ionic waters that were prepared by adding the SRNOM stock solution to Water 3 (ion-adjusted water). The concentrations of Mn^{2+} and other ions in Waters 1–14 were determined by using an inductively coupled plasma mass spectrometry system (HP-7800; Agilent Technologies, Inc., Santa Clara, California, USA) and an ion chromatography system (ICS-1000 and ICS-1100; Thermo Fisher Scientific Inc., Waltham, Massachusetts, USA), respectively. The alkalinity was determined by titration against 0.01 M H_2SO_4, whereas the turbidity, DOC, and ultraviolet absorbance at 260 nm (UV260) were measured by using a ratio turbidimetric determination method (2100Q Portable Turbidimeter, Hach Co., Loveland, Colorado, USA), a TOC analyzer (Model 900, Sievers Instruments, Boulder, Colorado, USA), and a spectrophotometer with a 5-cm cell (UV-1800; Shimadzu, Kyoto, Japan), respectively. As a pretreatment for the Mn^{2+}, other ions, DOC, and UV260 determinations, the waters were filtered through a

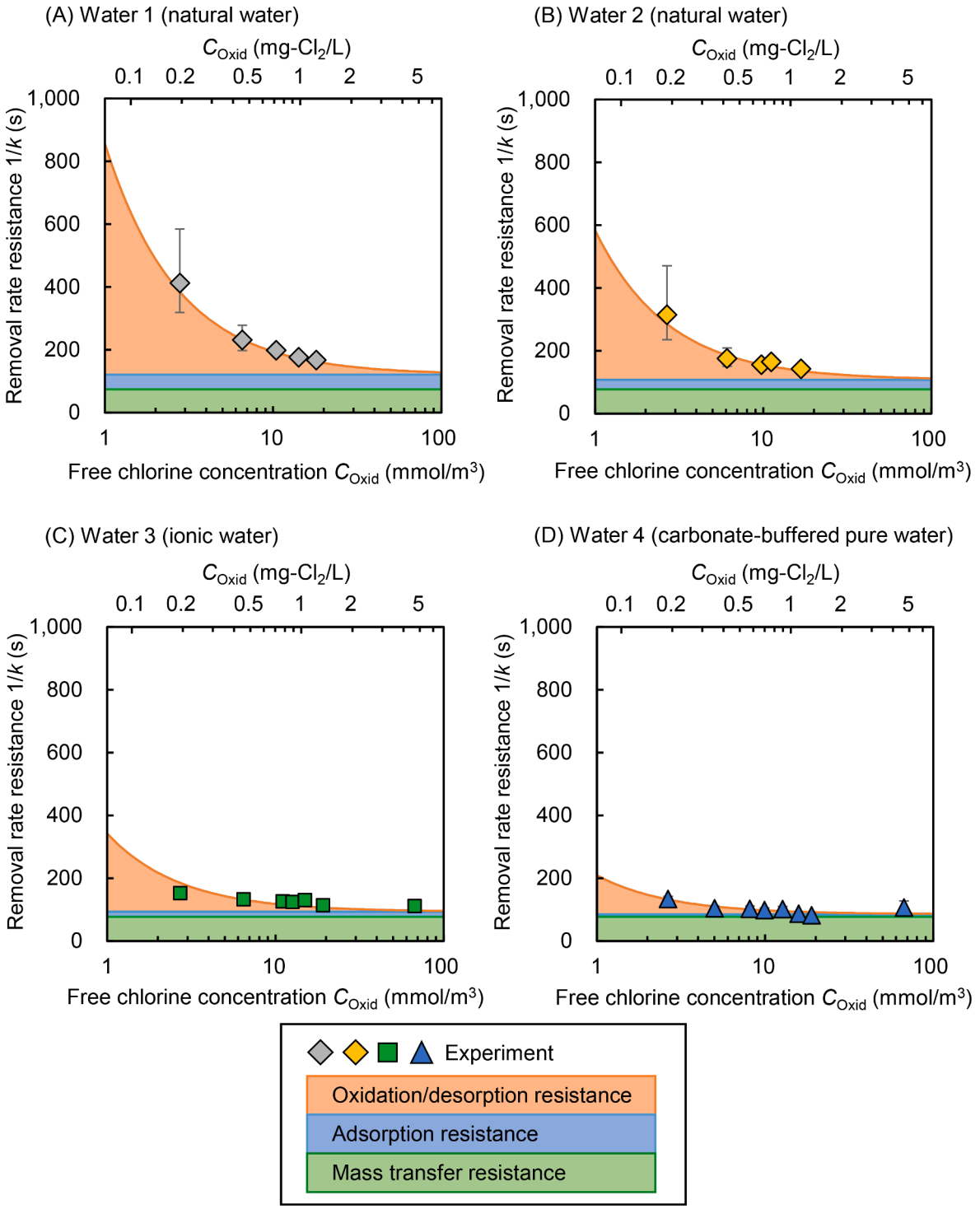

Fig. 2. Removal-rate resistance ($1/k$) and its components (i.e., rate resistances of external-film mass transfer, adsorption, and oxidation/desorption) versus free chlorine concentration. Results from Run 1 using Water 1 (A); Run 2, Water 2 (B); Run 3, Water 3 (C); and Run 4, Water 4 (D). SPAC-A1 was used as the carbon. Initial Mn^{2+} concentration, 7.7–10 μg/L (0.140–0.182 mmol/m^3); carbon dosage, 1.0 mg/L (1.0 g/m^3); water temperature, 19–20 °C; G, 509 s^{-1}. The experimental data for k and C_{Oxid} value determinations are shown in Fig. S3. Error bars indicate 95% confidence intervals. The values of component rate resistances were calculated from the components of Eq. (26) substituting the values of $1/Ak_F$, $1/Ak_AC_{Site}$, θ_C, and k_D/k_{Oxid} from Table 4.

membrane filter (0.2-μm pore size; DISMIC 25HP020AN).

3.3. Catalytic oxidative Mn^{2+} removal by carbon and chlorine in batch experiments

Transparent 1-L or 4-L polyvinyl-chloride beakers and a floating magnetic stirrer (Nalgene suspended magnetic stir bar; Thermo Fisher Scientific Inc.) were used for the batch experiments. For each experiment, 1000 mL or 2000 mL of a water sample was placed into a 1-L or 4-L beaker, respectively, and stirred at 50–800 rpm. Mixing intensity, G, was determined from the stirring speed, the projected area of the magnetic stirrer in the rotational direction, the water volume, and the viscosity, using Eq. (B.3): the G values were 23–1440 s^{-1}. Water temperature was 3–23 °C. One of the test carbons was added at 1.0 mg/L

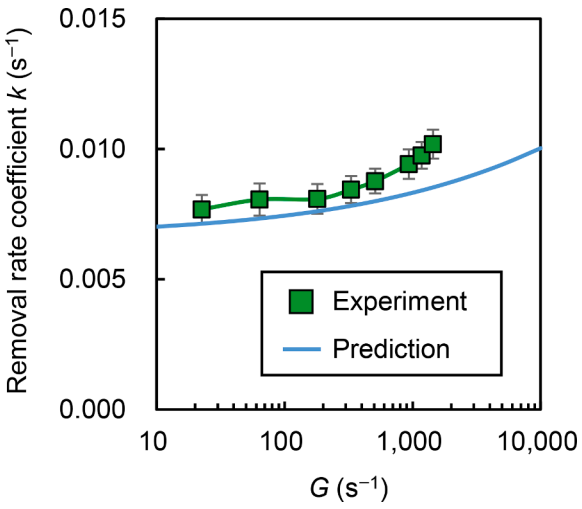

Fig. 3. Effect of mixing intensity (G) on removal-rate coefficient (k). Results from Run 7 using Water 3. SPAC-A1 was used as the carbon. Initial Mn^{2+} concentration, 10 μg/L (0.182 mmol/m^3); carbon dosage, 1.0 mg/L (1.0 g/m^3); free chlorine dosage, 1.00 mg-Cl_2/L (14.1 mmol/m^3); water temperature, 19–20 °C. The experimental data for the k value determination are shown in Fig. S7. Error bars indicate 95% confidence intervals. The prediction was generated by substituting the values of k_F and A from Eqs. (B.2) and (20), respectively, and the remaining parameters (Ak_AC_{Site}, θ_C, and k_D /k_{Oxid}) from Table 4.

after adjusting the pH of the water to neutral (6.9–7.0). After 5 min from the time of the carbon dose, free chlorine was added at 0.00–4.85 mg-Cl_2/L (0.00–68.4 mmol/m^3) to initiate the oxidative removal of Mn^{2+}. During the oxidative Mn^{2+}removal reaction, the pH of the water was kept neutral (6.9–7.1) by adding H_2SO_4 (0.05 mol/L) or HCl (0.10 mol/L) solution. NaOCl solution (Fujifilm Wako Pure Chemical Corporation) was diluted with ultrapure water to adjust the free chlorine concentration to 600–1000 mg-Cl_2/L (8.46–14.1 mol/m^3) and used as the source of free chlorine. Forty milliliters of water samples were withdrawn from the beaker every 2.5 min for 7.5 min, or at 1.0, 2.5, 4.0, 5.0, and 7.5 min, and immediately filtered through a membrane filter (0.2-μm pore size; DISMIC 25HP020AN). The Mn^{2+} and free chlorine concentrations in the filtrates were determined by inductively coupled plasma mass spectrometry (HP-7800; Agilent Technologies, Inc.) and the *N,N*-diethyl-*p*-phenylenediamine colorimetric method (DR. 900, Hach Co.), respectively. Table 3 summarizes the experimental conditions. Most experiments were conducted multiple times, confirming good reproducibility of the experimental results. Some of the experiments (Run 1, 2, and 8 and a part of Run 13) were conducted only once each, but 4–6 samplings were conducted in each experiment, providing multiple measurements.

4. Results and discussion

4.1. Effects of free chlorine and co-existing substances

From Eqs. (1), (18), and (25), the removal-rate coefficient (k), which can be determined from the experimental results, is expressed as a function of free chlorine concentration (C_{Oxid}):

$$\left(\frac{1}{k}\right) = \frac{1}{A}\left(\frac{1}{k_F}\right) + \frac{1}{A}\left(\frac{1}{k_A C_{Site}(1-\theta_C)}\right) + \frac{1}{A}\left(\frac{k_D}{k_{Oxid}k_A C_{Site}(1-\theta_C)}\right)\left(\frac{1}{C_{Oxid}}\right) \quad (26)$$

Eq. (26) tells us that 1) the reciprocal of the removal-rate coefficient ($1/k$, hereafter called removal-rate resistance) is a linear function of the reciprocal of free chlorine concentration ($1/C_{Oxid}$), and 2) both the slope of $1/k$ against $1/C_{Oxid}$ and the intercept of the linear function change depending on water quality, because co-existing substances competing for adsorption sites change the value of θ_C (the fractional adsorption-site coverage).

The validity of Eq. (26) was assessed on the basis of the results of experiments where Mn^{2+} was removed by the same SPAC in different waters under the same temperature and mixing conditions. The values of $1/k$ increased linearly with $1/C_{Oxid}$ (Fig. 1). Furthermore, both the slope and the intercept of the linear relationships were different depending on the water: they were smallest in Water 4 (carbonate-buffered pure water), followed by Water 3 (ionic water containing Ca^{2+} and other ions), and Waters 1 and 2 (natural waters).

We next determined the parameter values for Eq. (26) by using least-squares criteria to fit the experimental data: the parameter values were optimized to minimize the sum of the squared errors between the observed and calculated $1/k$ values. The parameters A, k_A, C_{Site}, k_D, and k_{Oxid} should have the same respective values when the same activated carbon is used, and the parameter k_F should have the same value when the same temperature and mixing conditions are applied to the same activated carbon. On the other hand, θ_C should differ between the waters tested, but it should be zero in Water 4 (carbonate-buffered pure water). Finally, the values of the parameters were uniquely determined as shown in Table 4. Note that the uniqueness of the determination was validated on the basis of theoretical considerations (see Appendix A). The solid lines in Fig. 1 shows the $1/k$ calculated by Eq. (26) after substituting the parameter values from Table 4. The solid lines are in close agreement to most of the plotted data, and the square of the correlation coefficient (r^2) between the experimental and calculated $1/k$ values was 0.97 (Fig. S4), indicating that Eq. (26) successfully expressed the effects of free chlorine concentration in different waters on the removal of Mn^{2+} by SPAC and free chlorine.

According to Eq. (26), the removal-rate coefficient comprises three group parameters, each presenting a rate resistance: the external-film mass transfer (first term on the right-hand side of Eq. (26)), adsorption (second term), and oxidation/desorption (third term). Fig. 2 shows the breakdown of the removal-rate resistance as a function of free chlorine concentration. The breakdowns were calculated from each term on the right-hand side of Eq. (26) by substituting the parameters from Table 4. It is very reasonable that the removal-rate resistance for oxidation/desorption increases with decreasing free chlorine concentration, which then decreases the removal-rate coefficient. The breakdown of the removal-rate resistances at a free chlorine concentration of 1.0 mg/L (14.1 mmol/m^3) in Water 1 (natural water, Fig. 2A) were 77.7, 46.6, and 58.0 s for mass transfer, adsorption, and oxidation/desorption, respectively, indicating that the mass-transfer resistance was the largest contributor, but also that all three resistances contributed roughly equally to the overall removal rate. In Water 2 (another natural water, Fig. 2B) these values were 77.7, 30.2, and 37.7 s. In contrast, in Water 4 (a carbonate-buffered pure water), they were 77.7, 7.9, and 9.8 s, respectively, indicating that the mass-transfer resistance was dominant in determining the overall removal rate (Fig. 2D). This is consistent with the previous finding that the removal-rate coefficient in carbonate-buffered pure water is predictable under the assumption that the external-film mass transfer is the rate-determining step (Saito et al., 2020).

The value of θ_C was set to zero for Water 4 because of the absence of competitive adsorption substances. The values of θ_C (the fractional adsorption-site coverage) were 83% and 74% for Waters 1 and 2 (natural waters), respectively. θ_C was 50% for Water 3, which has the same ionic composition as the natural waters. Considering the earlier finding that Ca^{2+} was the dominant ion influencing Mn^{2+} removal in water (Saito et al., 2022), we infer that the reduction of adsorption sites in the natural water was mostly due to Ca^{2+}. The difference in θ_C values between Waters 1 and 2 and Water 3 indicates that the natural organic matter (NOM) in these waters, another source of competitive adsorption substances (Saito et al., 2022), also reduced the adsorption sites by ~30%. The DOC of Water 1 and Water 2 was almost the same, but θ_C was greater in Water 1, indicating that the characteristics of the NOM

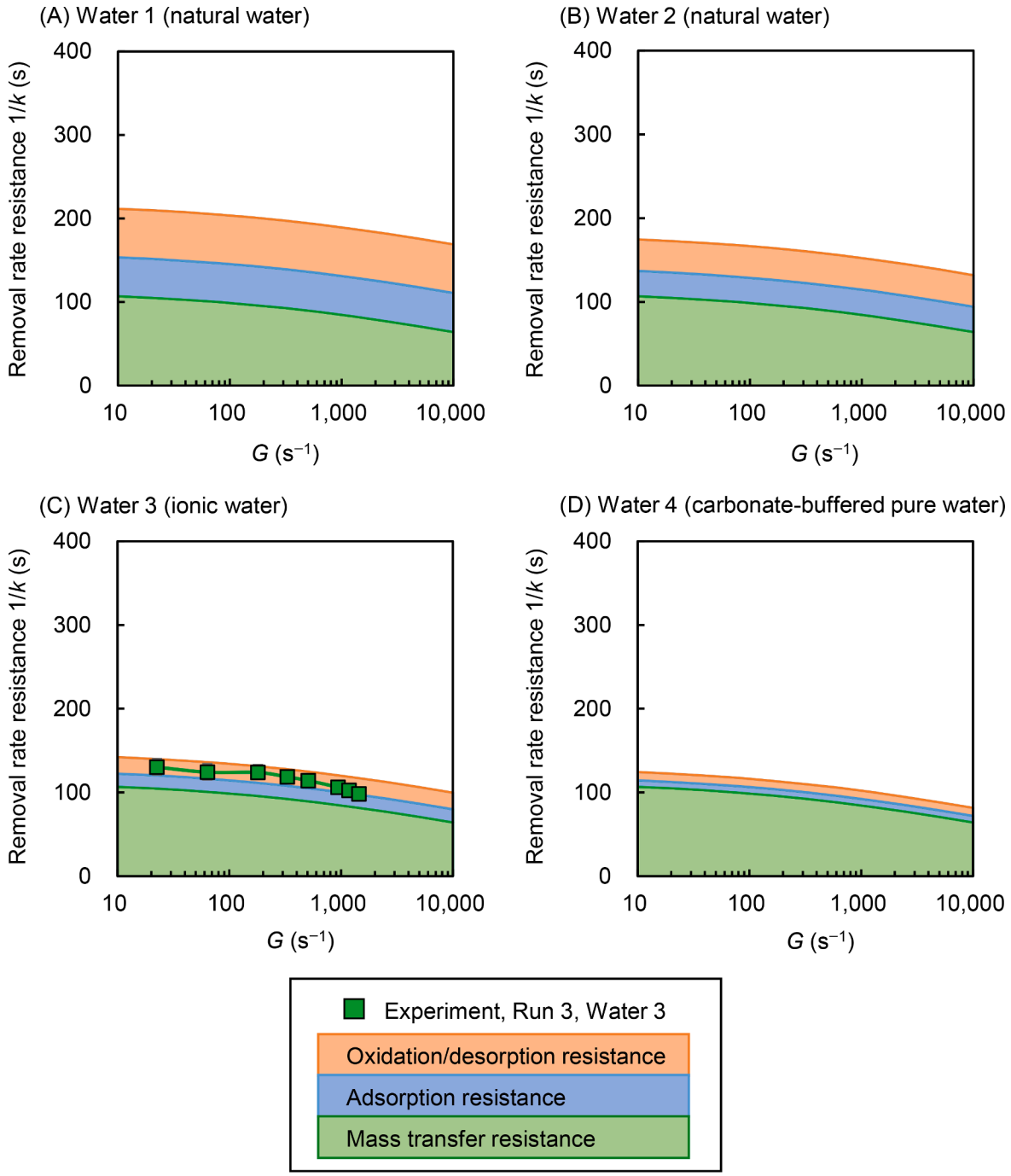

Fig. 4. Removal-rate resistance ($1/k$) broken into its components (i.e., rate resistances of external-film mass transfer, adsorption, and oxidation/desorption) versus mixing intensity (G). SPAC-A1 was used as the carbon. Initial Mn^{2+} concentration, 10 μg/L (0.182 mmol/m^3); carbon dosage, 1.0 mg/L (1.0 g/m^3); free chlorine dosage, 1.00 mg-Cl_2/L (14.1 mmol/m^3); water temperature, 19–20 °C. The experimental data for the k value determination are shown in Fig. S7. Error bars indicate 95% confidence intervals. The component rate resistances were predicted by substituting the values of k_F and A from Eqs. (B.2) and (20), respectively, and the others (Ak_AC_{Site}, θ_C, and k_D/k_{Oxid}) from Table 4.

influence the removal of Mn^{2+}. Alternatively, if the turbidity component inhibits Mn^{2+} removal, the relatively high turbidity of Water 1 could be another reason for the higher value of θ_C in Water 1. On the other hand, in experiments using the same NOM (SRNOM), the Mn^{2+} removal rate decreased with increasing NOM as well as Ca^{2+} concentrations (Saito et al., 2022), and the application of Eq. (26) to those data clearly revealed that the fractional percentage of remaining adsorption sites ($1-\theta_C$) actually decreased with increasing Ca^{2+} and SRNOM concentrations (Fig. S5). This demonstrates the excellent ability of the Eq. (26) to analyze Mn^{2+} removal phenomena.

The two-resistance model incorporating mass-transfer and oxidation rates has been applied in previous studies analyzing Mn^{2+} removal with a granular MnO_X catalyst (Bierlein et al., 2015; Kenari et al., 2019; Merkle et al., 1997). MnO_X would have a higher adsorption capacity for Mn^{2+} than activated carbon, which reduces the rate resistance of adsorption, and the particle size of MnO_X, which is much larger than SPAC/PAC, increases the mass-transfer resistance. Therefore, the application of the two-resistance model in the previous studies was probably reasonable and does not seem to be inconsistent with our study. Nevertheless, it would be useful to have a universal model

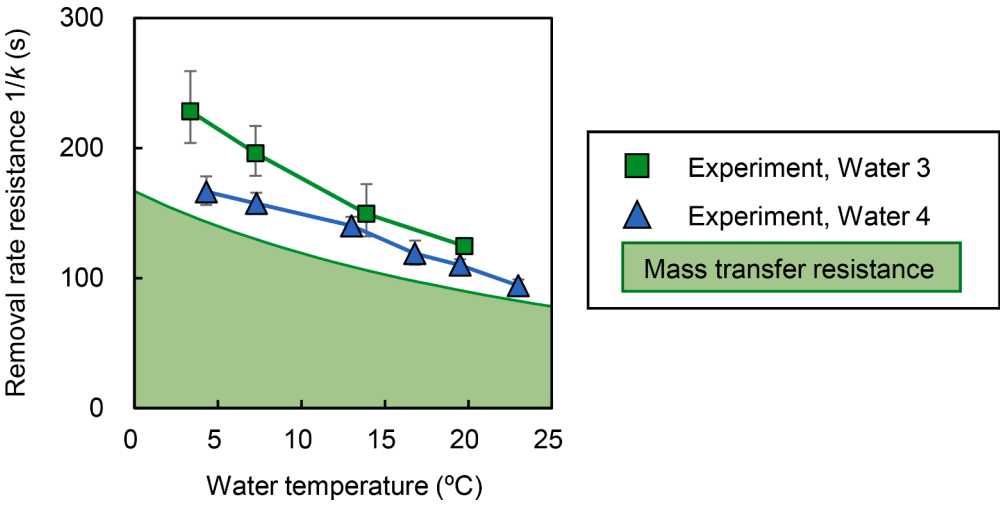

Fig. 5. Effect of water temperature on removal-rate resistance ($1/k$) and mass-transfer resistance ($1/Ak_F$). Results from Run 9 using Water 3 and Run 10 using Water 4. SPAC-A1 was used as the carbon. Initial Mn^{2+} concentration, 10 μg/L (0.182 mmol/m^3); carbon dosage, 1.0 mg/L (1.0 g/m^3); free chlorine dosage, 1.00 mg-Cl_2/L (14.1 mmol/m^3); G, 401–528 s^{-1}. The experimental data for the k value determination are shown in Fig. S10. Error bars indicate 95% confidence intervals. Values for A and k_F were predicted by Eqs. (20) and (B.2), respectively.

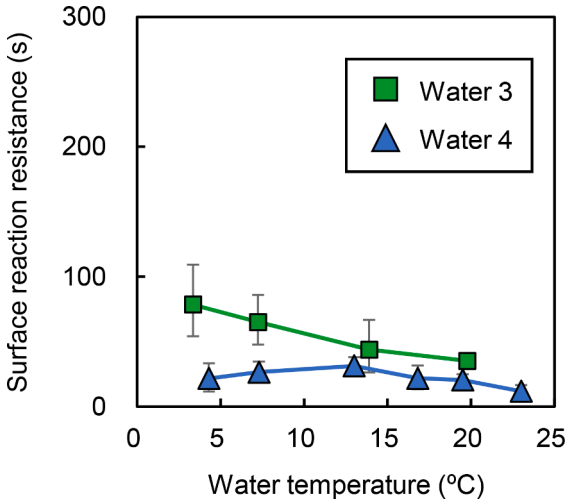

Fig. 6. Effect of water temperature on surface reaction resistance. Results from Run 9 using Water 3 and Run 10 using Water 4. SPAC-A1 was used as the carbon. Initial Mn^{2+} concentration, 10 μg/L (0.182 mmol/m^3); carbon dosage, 1.0 mg/L (1.0 g/m^3); free chlorine dosage, 1.00 mg-Cl_2/L (14.1 mmol/m^3); G, 401–528 s^{-1}. The values for surface reaction resistances were obtained by subtracting mass-transfer resistance ($1/Ak_F$) from the removal-rate resistance ($1/k$) in Fig. 5. Error bars indicate 95% confidence intervals.

describing the removal kinetics of Mn^{2+} by both MnO_X and activated carbon, which have very different catalytic activities and particle sizes.

4.2. Effect of mixing intensity

We investigated the effect of mixing intensity on the removal-rate coefficient (k) (Fig. 3). We plotted the experimental data, and a solid line showing the values predicted by Eq. (26), substituting the value of k_F from the mass-transfer-coefficient correlation equation (see Appendix B and Table S1), A from Eq. (20), and the remaining parameters (Ak_AC_{Site}, θ_C, and k_D/k_{Oxid}) from Table 4. The agreement between the experimental and predicted values further validates Eq. (26).

Both the experimental and predicted results indicate that the removal-rate coefficient increased with mixing intensity, but the rate of the increase in the experimental results became steeper in the range of $G > 1000\ s^{-1}$, deviating from the predicted rate coefficient values. We hypothesized that the steep increase behind the deviation was due to the disintegration of the activated-carbon particles—which were mildly aggregated at the time of dosing—under the high mixing intensity. The predictions were made under the assumption that the size of the activated-carbon particles, which were partially aggregated in the stock suspension, was maintained after dosing because in situ particle-size measurement was not possible. If this hypothesis is correct, such a steep increase in the removal-rate coefficient with mixing intensity in the high-G-value range should not be observed for activated-carbon particles that are already in a dispersed state at the time of dosing. To verify this hypothesis, we used non-aggregated activated carbon (SPAC-A2), whose particle size did not change between before and after the dispersion treatment (3.15 vs. 3.01 μm), and we conducted batch experiments for Mn^{2+} removal at different mixing intensities. We did not observe the same steep increase in the removal-rate coefficient with increasing mixing intensity for SPAC-A2 (Fig. S8), strongly suggesting that the steep increase observed for SPAC-A1 was due to particle disintegration by the high mixing conditions.

We broke down the removal-rate resistance ($1/k$) against mixing intensity into the three resistance components (i.e., rate resistances from external-film mass transfer, adsorption, and oxidation/desorption; Fig. 4). The effect of high mixing intensity on Mn^{2+} removal rate was large in carbonate-buffered pure water, but it was smaller in natural water because mass-transfer resistance was not a dominant contributor. This suggests that the effect of flow rate on Mn removal in flow reactor, which is installed prior to membrane filtration process in practice, can be evaluated roughly as a change in HRT (hydraulic retention time) because the effect of G-value (turbulent mixing intensity) change with flow rate change is small.

4.3. Effect of water temperature

We investigated the effect of water temperature on the removal-rate resistances ($1/k$) (Fig. 5). We also separated out the mass-transfer resistance (one component of removal-rate resistances) predicted by the mass-transfer-coefficient correlation equation (see Appendix B and Table 1S), which was validated in Section 4.2. The adsorption and oxidation/desorption components are not depicted because the temperature effects were not predictable. As water temperature increased, the viscosity decreased, so the mass-transfer resistance decreased. On the other hand, the removal-rate resistance, of which mass-transfer resistance is one of the components, also decreased. We therefore consider the temperature dependence of the removal-rate resistance to be due to the temperature dependence of the mass-transfer resistance.

By subtracting the mass-transfer resistance from the total removal-rate resistance, the magnitudes of the other components, i.e., adsorption and oxidation/desorption resistances (hereafter referred to as the

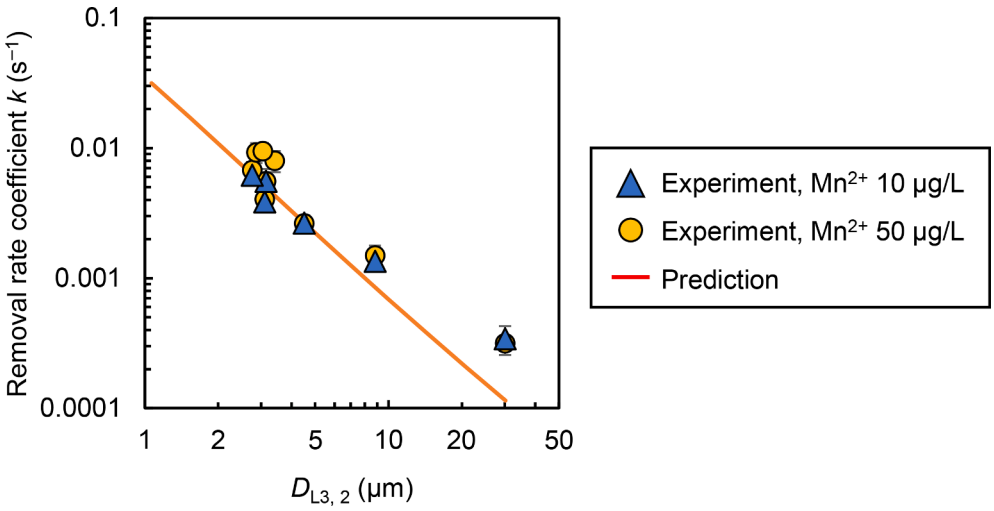

Fig. 7. Effect of particle size of activated carbon ($D_{L3,2}$) on removal-rate coefficient (k). Results from Run 11 using Water 5 (Mn^{2+}, 10 μg/L: 0.182 mmol/m^3) and Run 12 using Water 6 (Mn^{2+}, 50 μg/L: 0.910 mmol/m^3). Nine different activated carbons originating from PAC-B were used. Carbon dosage, 1.0 mg/L (1.0 g/m^3); free chlorine dosage, 1.00 mg-Cl_2/L (14.1 mmol/m^3); water temperature, 19–20 °C; G, 360 s^{-1}. The experimental data for the k value determination are shown in Fig. S11. Error bars indicate 95% confidence intervals. The prediction used Eq. (26), substituting the values of A and k_F from Eqs. (20) and (B.2), respectively, and $1/k_A C_{Site}$ and k_D/k_{Oxid} from Table 4.

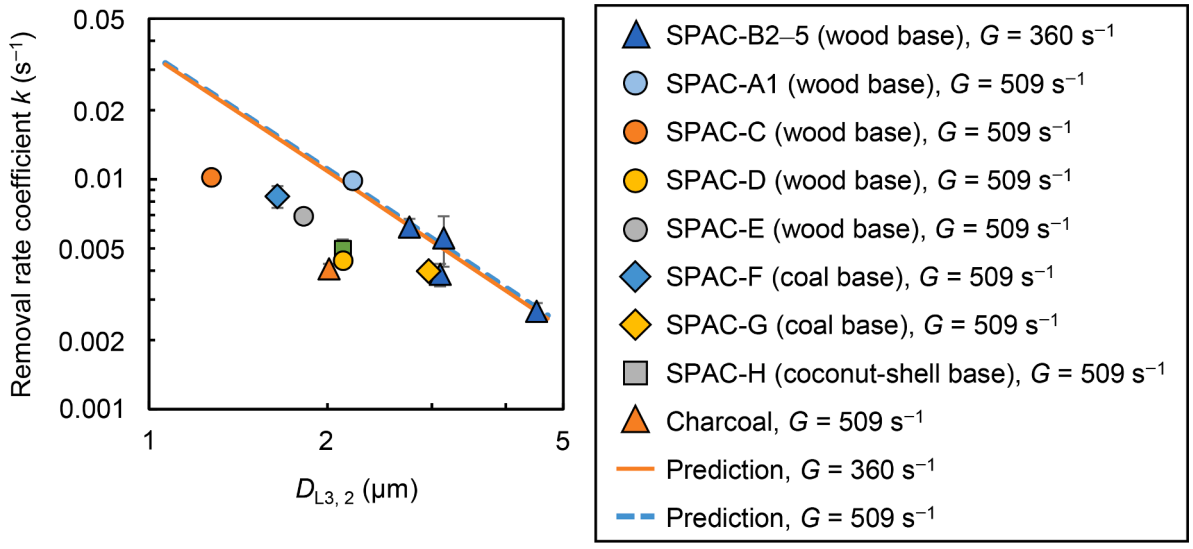

Fig. 8. Removal-rate coefficient (k) values for various activated carbons and charcoal. Results from Runs 1 and 13 using Water 4, and Run 11 using Water 5. Twelve activated carbons with $D_{L3,2}$ from 1 to 5 μm were used. Initial Mn^{2+} concentration, 10 μg/L (0.182 mmol/m^3); carbon dosage, 1.0 mg/L (1.0 g/m^3); free chlorine dosage, 1.00 mg-Cl_2/L (14.1 mmol/m^3); water temperature, 19–20 °C. G, 360 s^{-1} or 509 s^{-1}. The experimental data for the k value determination are shown in Figs. S11 and S12. Error bars indicate 95% confidence intervals. The prediction used Eq. (26), substituting the values of A and k_F from Eqs. (20) and (B.2), respectively, and $1/k_A C_{Site}$ and k_D/k_{Oxid} from Table 4.

surface reaction resistance), were elucidated and plotted against water temperature (Fig. 6). In Water 4 (carbonate-buffered pure water), the surface reaction resistance ranged from 12 to 31 s without a clear increasing or decreasing trend with water temperature. On the other hand, the surface reaction resistance in Water 3 (ionic water) clearly increased with decreasing water temperature. The parameters relating to the surface reaction resistance are $k_A C_{Site}$, k_D/k_{Oxid}, and θ_C in Eq. (26). Among these, θ_C is zero in Water 4 (carbonate-buffered pure water) as described in Section 4.1, and therefore the lack of a temperature dependence of the surface reaction resistance in Water 4 indicates that $k_A C_{Site}$ and k_D/k_{Oxid} are probably not affected by temperature. Thus, the temperature dependence of surface reaction resistance observed in Water 3 indicates that θ_C (the fraction of adsorption sites occupied by co-existing substances, mainly Ca^{2+}, as described in Section 4.1) increased with decreasing temperature. This is consistent with some previous sorption studies using zeolite and kaolinite (Aragaw and Ayalew, 2019), in that Ca^{2+} adsorption is enhanced with decreasing temperature. However, note that there are also other studies reporting that Ca^{2+} adsorption is enhanced with increasing temperature (Borhade and Kankrej, 2017; Wang et al., 2021; Xue et al., 2014). We therefore consider that the changes in the surface reaction resistance with water temperature in Water 3 can be explained by the increase of θ_C due to enhanced Ca^{2+} adsorption at low water temperature. In Water 4, θ_C was zero at all temperatures, so there was no temperature-dependent change in surface reaction resistance.

These observations suggest that the decrease in Mn^{2+} removal rate with decreasing water temperature is caused not only by the decrease in mass-transfer rate from the increase in viscosity, but also by the increase in adsorption of co-existing substances, mainly Ca^{2+}, on the activated carbon, which decreases the available adsorption sites for Mn^{2+}.

4.4. *Effect of activated-carbon particle size*

We compared the Mn^{2+} removal-rate coefficients (k) against the particle size of activated carbon (Fig. 7). We plotted the experimental data using carbon particles of nine sizes originating from the same carbon for comparison with the prediction by Eq. (26). The experimental and predicted values were almost in agreement, and both showed a

linear relationship on a double logarithmic plot (a power relationship). A closer look shows that the predicted values had a steeper slope than the experimental values, and the experimental values were somewhat greater than the predicted ones in the range of larger particles. This could be due to any difference in particle shape or surface property: we assumed a series of parameter values, including a sphericity value, independent of particle size for these predictions (Armenante and Kirwan, 1989), but in actual activated carbon, these values could have varied with particle size. Overall, the particle size of the activated carbon strongly affects the Mn^{2+} removal performance.

4.5. Effect of activated-carbon species

We plotted the experimental values for the removal-rate coefficient (k) for eleven different activated carbons and a charcoal without any activation treatment against their particle sizes (Fig. 8). Although the carbon species were different, we observed a rough trend of decreasing k values with increasing particle size, which is the same as predicted for particles of the same type of carbon in Section 4.4.

Focusing on the variation of individual carbon species, the k values of two wood-based activated carbons of similar particle size (SPAC-A1, $D_{L3,2} = 2.21$ μm; SPAC-D, $D_{L3,2} = 2.13$ μm) were 0.0091 s^{-1} and 0.0044 s^{-1}, respectively, differing by a factor of 2.1. The charcoal differed from the activated carbon (SPAC-A1) by a factor of 2.2 even though their particle sizes were similar. If we assumed that these individual variations were solely due to the concentration of adsorption sites (C_{Site}) and applied Eqs. (26), (20), and (B.2), the values for C_{Site} varied by a factor of 8 across the activated carbons and charcoal. There was no clear tendency for the activated carbons, with larger internal surface area (~1000 m^2/g) (Matsui et al., 2015), to have clearly higher Mn^{2+} removal rates than the charcoal before the activation process (<400 m^2/g) (Hitomi et al., 1993; Sontheimer et al., 1988), but this is consistent with previous findings that Mn^{2+} removal reactions occur on the outer surface of activated-carbon particles (Saito et al., 2020). Coconut-shell-based and coal-based activated carbons reportedly have lower oxygen contents, implying lower polarity, than wood-based activated carbon (Matsui et al., 2015; Pan et al., 2017; Partlan et al., 2016; Pendleton et al., 2002). However, there was no clear trend toward superiority or inferiority of activated carbon from any of the raw materials with respect to Mn^{2+} removal. The relationship between carbon properties and Mn^{2+} removal—specifically, the competitive adsorption of Mn^{2+}—awaits further study, but these findings suggest that the Mn^{2+} removal performance could be maximized by selecting suitable raw materials at the procurement stage and/or optimizing the activation condition during manufacture. It should be noted, however, that the effect of carbon particle size is more crucial than carbon properties, such that the k value of 2-μm carbon was 12–27 times that of 30-μm carbon (Fig. 7).

5. Conclusions

We derived a kinetic model for the removal of a trace substance by catalytic oxidation on a solid catalyst surface. Applying the derived model, we quantitatively analyzed the oxidative removal rate of a trace concentration of Mn^{2+} by activated carbon as a catalyst in the presence of free chlorine.

(1) By introducing the external-film mass-transfer resistance model, the surface reaction model of the Eley-Rideal mechanism, the quasi-steady-state approximation, and the assumption that the concentration of an oxidation target substance is much lower than that of an oxidant, we were able to derive an overall removal kinetic model with a first-order reaction formula in which the removal-rate coefficient is represented by a linear combination of the three rate resistances, i.e., those from external-film mass transfer, adsorption, and oxidation/desorption. The contributions of each resistance could be easily evaluated. The equations for the batch reaction are as follows:

$$\frac{dC_M}{dt} = -K_R\, AC_M$$

$$\frac{1}{K_R} \equiv \frac{1}{k_F} + \frac{1}{k_A C_{Site}(1-\theta_C)} + \frac{k_D}{k_A k_{Oxid} C_{Site}(1-\theta_C)} \frac{1}{C_{Oxid}}$$

(2) The model fit well all the experimental results for the Mn^{2+} removal-rate coefficients under varying water quality, free chlorine concentration, mixing intensity, water temperature, and activated-carbon particle size.
(3) Under practical conditions for Mn^{2+} removal, i.e., natural water containing Mn^{2+} at 10 μg/L, free chlorine concentration of 1.0 mg-Cl_2/L, mixing intensity of 509 s^{-1}, and water temperature of 20 °C, the removal-rate resistances from external-film mass transfer, adsorption, and oxidation/desorption were 77.7, 46.6, and 58.0 s, respectively, and their contributions to the removal rate were roughly equal.
(4) In water with no competing substances, the effect of water temperature on the Mn^{2+} removal rate can be explained by changes in water viscosity, which affects the mass-transfer coefficient. In the equation above, $k_A C_{Site}$ and k_D/k_{Oxid}, which are related to adsorption, desorption, and oxidation, would likely not be affected by temperature.
(5) The effect of co-existing substances was analyzed quantitatively as a decrease in available adsorption sites for Mn^{2+} on the activated-carbon surface. A 50% decrease in the concentration of adsorption sites by the competitive cation Ca^{2+}, present in water at a concentration of 0.26 mmol/L, resulted in a 15% decrease in the Mn^{2+} removal rate. The reduction in adsorption sites by a competitive cation would become greater at lower water temperature. Therefore, under low water temperature conditions, the removal rate of Mn^{2+} is greatly reduced because of the enhanced competitive cation adsorption in addition to the decrease in mass-transfer rate due to increased viscosity.
(6) Activated carbons and charcoal had an 8-fold difference in adsorption-site concentrations, which resulted in removal-rate coefficients that differed by a factor of 2.2. However, the carbon particle size in water is a more crucial factor for the removal-rate coefficient.

Declaration of Competing Interest

The authors declare that they have no known competing financial interests or personal relationships that could have appeared to influence the work reported in this paper.

Acknowledgments

The authors gratefully acknowledge Futamura Chemical Co., Ltd. (Nagoya, Japan), Osaka Gas Chemicals Co., Ltd. (Osaka, Japan), Dainen Co., Ltd. (Himeji, Japan), and Kuraray Co., Ltd. (Osaka, Japan) for providing powdered activated-carbon samples. The present work, however, has not been evaluated by these entities and does not necessarily reflect their opinion; therefore, no official endorsement should be inferred.

Funding

This work was supported by the Japan Society for the Promotion of Science [grant number 21K18736].

Supplementary materials

Supplementary material associated with this article can be found, in the online version, at doi:10.1016/j.wroa.2022.100153.

Appendix A

Iterating Eq. (26).

$$\left(\frac{1}{k}\right) = \left(\frac{1}{k_F} + \frac{1}{k_A C_{Site}(1-\theta_C)}\right)\frac{1}{A} + \left(\frac{k_D}{k_{Oxid} k_A C_{Site}(1-\theta_C)}\right)\frac{1}{A}\left(\frac{1}{C_{Oxid}}\right) \tag{A.1}$$

Eq. (A.1) describes a linear function of $1/k$ and $1/C_{Oxid}$. When this linear relationship is experimentally obtained, the values for I and S defined in the following equations are given by its intercept and slope, respectively (see Fig. A.1).

$$I \equiv \left(\frac{1}{k_F} + \frac{1}{k_A C_{Site}(1-\theta_C)}\right)\frac{1}{A} \tag{A.2}$$

$$S \equiv \left(\frac{1}{k_A C_{Site}(1-\theta_C)}\frac{k_D}{k_{Oxid}}\right)\frac{1}{A} \tag{A.3}$$

The parameters k_F, A, $k_A C_{Site}$, and k_D/k_{Oxid} should have the same values under the same temperature and mixing conditions with the same activated carbon. On the other hand, by conducting experiments using three types of water, with concentrations of competitive adsorption substances (Ca^{2+}, Mg^{2+}, and NOM) that include zero, a total of six values are obtained: three values each for I and S. The value for A (the external-film area of a catalyst per volume of water) is determined from independent measurements of physical properties of the activated carbon. There are five parameters (or grouped parameters) in the model remaining to be determined: k_F, $k_A C_{Site}$, k_D/k_{Oxid}, and two θ_C values (θ_{C1} and θ_{C2}, for two of the waters. $\theta_C = 0$ for the third water because the concentrations of Ca^{2+}, Mg^{2+}, and NOM are zero). There are five explanatory variables and six samples to use for their determination (three I values and three S values); hence there is one degree of freedom. Furthermore, values for I and S differed by experiment (Fig. 1). The explanatory variables can therefore be uniquely determined by the least-squares criterion to minimize the error of $1/k$.

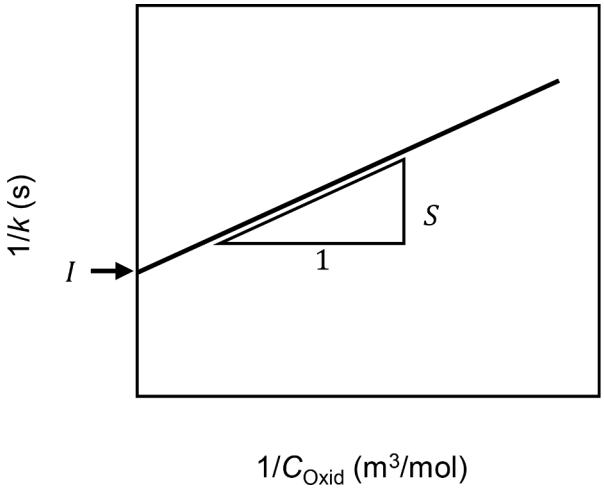

Fig. A.1. Ideal representation of the linear relationship between $1/k$ and $1/C_{Oxid}$.

Appendix B

Equation for the prediction of the external-film mass-transfer coefficient

Armenante and Kirwan (1989) have reported the following mass-transfer-coefficient correlation equation derived from their experiments using microparticles:

$$Sh \equiv \frac{k_F D_S}{D_W} = 2 + 0.52\left(\frac{D_S^{4/3}\varepsilon^{1/3}}{\sigma}\right)^{0.52}\left(\frac{\sigma}{D_W}\right)^{1/3} \tag{B.1}$$

Substituting Eq. (24) into Eq. (B.1) results in the following equation for the external-film mass-transfer coefficient:

$$k_F = \frac{D_W}{\varphi \varnothing D_{L3,2}} \left[2 + 0.52 \left(\frac{\left(\varphi \varnothing D_{L3,2}\right)^{4/3} G^{2/3}}{\sigma^{2/3}} \right)^{0.52} \left(\frac{\sigma}{D_W} \right)^{1/3} \right] \quad \text{(B.2)}$$

The relationship between ε and G is expressed as

$$G = \sqrt{\frac{\varepsilon}{\sigma}} \quad \text{(B.3)}$$

References

Ahumada, E., Lizama, H., Orellana, F., Suárez, C., Huidobro, A., Sepúlveda-Escribano, A., Rodríguez-Reinoso, F., 2002. Catalytic oxidation of Fe(II) by activated carbon in the presence of oxygen. Effect of the surface oxidation degree on the catalytic activity. Carbon N. Y. 40, 2827–2834.

Al-Sakkari, E.G., El-Sheltawy, S.T., Attia, N.K., Mostafa, S.R., 2017. Kinetic study of soybean oil methanolysis using cement kiln dust as a heterogeneous catalyst for biodiesel production. Appl. Catal. B Environ. 206, 146–157.

Aragaw, T.A., Ayalew, A.A., 2019. Removal of water hardness using zeolite synthesized from Ethiopian kaolin by hydrothermal method. Water Pract. Technol. 14, 145–159.

Armenante, P.M., Kirwan, D.J., 1989. Mass transfer to microparticles in agitated systems. Chem. Eng. Sci. 44, 2781–2796.

Baxter, R.J., Hu, P., 2002. Insight into why the Langmuir-Hinshelwood mechanism is generally preferred. J. Chem. Phys. 116, 4379–4381.

Bierlein, K.A., Knocke, W.R., Tobiason, J.E., Subramaniam, A., Pham, M., Little, J.C., 2015. Modeling manganese removal in a pilot-scale postfiltration contactor. J. Am. Water Works Assoc. 107, E109–E119.

Borhade, A.V., Kankrej, S.R., 2017. An efficient cost-effective removal of Ca2+, Mg2+, and Cu2+ ions from aqueous medium using Chlorosodalite synthesized from coal fly ash. J. Chem. Eng. 62, 596–607.

Boudart, M., Djega-Mariadassou, G., 2014. Kinetics of Heterogeneous Catalytic Reactions. Princeton University Press, Princeton, NJ, USA.

Carlson, K.H., Knocke, W.R., Gertig, K.R., 1997. Optimizing treatment through Fe and Mn fractionation. J. /Am. Water Work. Assoc. 89, 162–171.

Chantrasa, A., Phlernjai, N., Goodwin, J.G., 2011. Kinetics of hydrotalcite catalyzed transesterification of tricaprylin and methanol for biodiesel synthesis. Chem. Eng. J. 168, 333–340.

Chorkendorff, I.(Ib), Niemantsverdriet, J.W., 2007. Concepts of Modern Catalysis and Kinetics. Wiley-VCH, Weinheim, Germany.

Civardi, J., Tompeck, M., 2015. Iron and Manganese Removal Handbook. American Water Works Association, Denver, CO, USA.

Dhawane, S.H., Al-Sakkari, E.G., Kumar, T., Halder, G., 2021. Comprehensive elucidation of the apparent kinetics and mass transfer resistances for biodiesel production via in-house developed carbonaceous catalyst. Chem. Eng. Res. Des. 165, 192–206.

Ercan, C., Dautzenberg, F.M., Yeh, C.Y., Barner, H.E., 1998. Mass-transfer effects in liquid-phase alkylation of benzene with zeolite catalysts. Ind. Eng. Chem. Res. 37, 1724–1728.

Eshel, G., Levy, G.J., Mingelgrin, U., Singer, M.J., 2004. Critical Evaluation of the Use of Laser Diffraction for Particle-Size Distribution Analysis. Soil Sci. Soc. Am. J. 68, 736–743.

Faria, P.C.C., Órfão, J.J.M., Pereira, M.F.R., 2009. Activated carbon and ceria catalysts applied to the catalytic ozonation of dyes and textile effluents. Appl. Catal. B Environ. 88, 341–350.

Gerke, T.L., Little, B.J., Barry Maynard, J., 2016. Manganese deposition in drinking water distribution systems. Sci. Total Environ. 541, 184–193.

Gomes, H.T., Miranda, S.M., Sampaio, M.J., Silva, A.M.T., Faria, J.L., 2010. Activated carbons treated with sulphuric acid: catalysts for catalytic wet peroxide oxidation. Catal. Today 151, 153–158.

Gómez-Marín, A.M., Hernández-Ortiz, J.P., 2014. Langmuir-Hinshelwood mechanism including lateral interactions and species diffusion for CO electro-oxidation on metallic surfaces. J. Phys. Chem. C 118, 2475–2486.

Hatziantoniou, V., Andersson, B., Schöön, N.H., 1986. Mass transfer and selectivity in liquid-phase hydrogenation of nitro compounds in a monolithic catalyst reactor with segmented gas-liquid flow. Ind. Eng. Chem. Process Des. Dev. 25, 964–970.

Hitomi, M., Kera, Y., Tatsumoto, H., Ikuta, N., Kawafune, I., Abe, I., 1993. Evaluation of adsorption property of porous carbon materials (II). TANSO 156, 22–28 in Japanese.

Hu, P.Y., Hsieh, Y.H., Chen, J.C., Chang, C.Y., 2004. Adsorption of divalent manganese ion on manganese-coated sand. J. Water Supply Res. Technol. - AQUA 53, 151–158.

Jones, A., Murayama, M., Knocke, W.R., 2018. Incorporating aluminum species in MnO x (s) coatings on water filtration media. AWWA Water Sci. 1, e1114.

Kenari, S.L.D., Shabanian, J., Barbeau, B., 2019. Dynamic modeling of manganese removal in a pyrolusite fluidized bed contactor. Water Res. 154, 125–135.

Knocke, W.R., Occiano, S.C., Hungate, R., 1991. Removal of soluble manganese by oxide-coated filter media. Sorption rate and removal mechanism issues. J. Am. Water Work. Assoc. 83, 64–69.

Li, G., Hao, H., Zhuang, Y., Wang, Z., Shi, B., 2019a. Powdered activated carbon enhanced Manganese(II) removal by chlorine oxidation. Water Res. 156, 287–296.

Li, G., Ma, X., Chen, R., Yu, Y., Tao, H., Shi, B., 2019b. Field studies of manganese deposition and release in drinking water distribution systems: insight into deposit control. Water Res. 163.

Matsui, Y., Nakao, S., Sakamoto, A., Taniguchi, T., Pan, L., Matsushita, T., Shirasaki, N., 2015. Adsorption capacities of activated carbons for geosmin and 2-methylisoborneol vary with activated carbon particle size: effects of adsorbent and adsorbate characteristics. Water Res. 85, 95–102.

Merkle, P.B., Knocke, W.R., Gallagher, D., Little, J.C., 1997. Dynamic Model for Soluble Mn2+ Removal by Oxide-Coated Filter Media. J. Environ. Eng. 123, 650–658.

Misono, M., 2013. Heterogeneous Catalysis of Mixed oxides : Perovskite and Heteropoly Catalysts, 1st ed. Elsevier, Amsterdam, The Netherlands.

Moreno-Castilla, C., López-Ramón, M.V., Carrasco-Marín, F., 2000. Changes in surface chemistry of activated carbons by wet oxidation. Carbon N Y 38, 1995–2001.

Nakanishi, H., 1967. Kinetics of Continuous Removal of Manganese in a MnO2- Coated Sand Bed. Kogyo Kagaku Zasshi (J. Chem. Soc. Japan) 70 (4) in Japanese.

Pan, L., Nishimura, Y., Takaesu, H., Matsui, Y., Matsushita, T., Shirasaki, N., 2017. Effects of decreasing activated carbon particle diameter from 30 Mm to 140 nm on equilibrium adsorption capacity. Water Res. 124, 425–434.

Partlan, E., Davis, K., Ren, Y., Apul, O.G., Mefford, O.T., Karanfil, T., Ladner, D.A., 2016. Effect of bead milling on chemical and physical characteristics of activated carbons pulverized to superfine sizes. Water Res. 89, 161–170.

Pendleton, P., Wu, S.H., Badalyan, A., 2002. Activated carbon oxygen content influence on water and surfactant adsorption. J. Colloid Interface Sci. 246, 235–240.

Prins, R., Wang, A., Li, X., 2016. Introduction to Heterogeneous Catalysis, Advanced Textbooks in Chemistry. World Scientific Publishing, Singapore.

Riddick, T.M., Lindsay, N.L., Tomassi, A., 1958. Iron and Manganese in Water Supplies. J. Am. Water Works Assoc. 50, 688–696.

Ross, J.R.H., 2012a. The Kinetics and Mechanisms of Catalytic Reactions, in: Heterogeneous Catalysis. Elsevier, Amsterdam, The Netherlands, pp. 123–142.

Ross, J.R.H., 2012b. Large-Scale Catalytic Reactors, in: Heterogeneous Catalysis. Elsevier, Amsterdam, The Netherlands, pp. 143–169.

Saito, S., Matsui, Y., Shirasaki, N., Matsushita, T., 2022. Factors affecting the catalytic oxidative removal of soluble manganese in natural water by superfine powdered activated carbon and free chlorine. J. Water Process Eng. 49, 103007.

Saito, S., Matsui, Y., Yamamoto, Y., Matsushita, S., Mima, S., Shirasaki, N., Matsushita, T., 2020. Oxidative removal of soluble divalent manganese ion by chlorine in the presence of superfine powdered activated carbon. Water Res. 187, 116412.

Satterfield, C.N., 1969. Mass Transfer in Heterogeneous Catalysis. M.I.T. Press, Cambridge, MA, USA.

Singer, P.C., Reckhow, D.A., 2011. Chapter 7 Chemical oxidation. Ed.. In: Edzwald, James K. (Ed.), Water Quality and Treatment: A Handbook On Drinking Water. McGraw-Hill, Manhattan, NY, USA.

Sly, L.I., Hodgkinson, M.C., Arunpairojana, V., 1990. Deposition of manganese in a drinking water distribution system. Appl. Environ. Microbiol. 56, 628–639.

Sontheimer, H., Crittenden, J.C., Summers, R.S., 1988. Activated Carbon for Water Treatment, First. ed. DVGW-Forschungsstelle, Engler-Bunte-Institut. Universitat Karlsruhe (TH), Karlsruhe, Germany.

Takaesu, H., Matsui, Y., Nishimura, Y., Matsushita, T., Shirasaki, N., 2019. Micro-milling super-fine powdered activated carbon decreases adsorption capacity by introducing oxygen/hydrogen-containing functional groups on carbon surface from water. Water Res. 155, 66–75.

Tobiason, J.E., Bazilio, A., Goodwill, J., Mai, X., Nguyen, C., 2016. Manganese removal from drinking water sources. Curr. Pollut. Rep. 2, 168–177.

Tobiason, J.E., Knocke, W.R., Goodwill, J., Hargette, P., Bouchard, R., Zuravnsky, L., 2008. Characterization and Performance of Filter Media For Manganese Control. The Wate Research Foundation, Denver, CO, USA.

Wang, Z., Feng, Z., Yang, L., Wang, M., 2021. Effective removal of calcium and magnesium ions from water by a novel alginate–citrate composite aerogel. Gels 7 (3), 125.

Xue, Z., Li, Z., Ma, J., Bai, X., Kang, Y., Hao, W., Li, R., 2014. Effective removal of Mg2+ and Ca2+ ions by mesoporous LTA zeolite. Desalination 341, 10–18.

Zhao, Y., Kitajima, R., Shirasaki, N., Matsui, Y., Matsushita, T., 2020. Precoating membranes with submicron super-fine powdered activated carbon after coagulation prevents transmembrane pressure rise: straining and high adsorption capacity effects. Water Res. 177, 115757.